Journal of ELECTRONIC MATERIALS, Vol. 46, No. 10, 2017
DOI: 10.1007/s11664-017-5611-9

Barrier Parameters and Current Transport Characteristics of Ti/*p*-InP Schottky Junction Modified Using Orange G (OG) Organic Interlayer

K. SREENU,[1] C. VENKATA PRASAD,[1] and V. RAJAGOPAL REDDY[1,2]

1.—Department of Physics, Sri Venkateswara University, Tirupati 517 502, India. 2.—e-mail: reddy_vrg@rediffmail.com

A Ti/Orange G/*p*-InP metal/interlayer/semiconductor (MIS) junction has been prepared with Orange G (OG) organic layer by electron beam evaporation and spin coating processes. The electrical properties of Ti/*p*-InP metal/semiconductor (MS) and Ti/OG/*p*-InP MIS junctions have been analyzed based on current–voltage (*I*–*V*) and capacitance–voltage (*C*–*V*) characteristics. The MIS junction exhibited higher rectifying behavior than the MS junction. The higher barrier height (BH) of the MIS junction compared with the MS junction indicates effective modification by the OG layer. Also, the BH, ideality factor, shunt resistance, and series resistance were extracted based on the *I*–*V* characteristic, Cheung's and Norde's methods, and the Ψ_S–*V* plot. The BH evaluated by Cheung's and Norde's methods and the Ψ_S–*V* plot was shown to be similar, confirming the reliability and validity of the methods applied. The extracted interface state density (N_{SS}) of the MIS junction was less than for the MS junction, revealing that the OG organic layer reduced the N_{SS} value. Analysis demonstrated that, in the lower bias region, the reverse current conduction mechanism was dominated by Poole–Frenkel emission for both the MS and MIS junction. Meanwhile, in the higher bias region, Schottky emission governed the reverse current conduction mechanism. The results suggest that such OG layers have potential for use in high-quality electronic devices.

Key words: Orange G organic interlayer, *p*-type InP, MIS junction, electrical characteristics, interface state density, current transport properties

INTRODUCTION

Due to advances in semiconductor technology, metal/semiconductor (MS) junctions play an important role in development of semiconductor electronic devices. However, achieving low ideality factor in MS junctions with an interfacial layer is critical for use in electronic devices. To realize such progressive devices, organic materials can be employed as contacts to inorganic semiconductors to maintain the barrier height, especially at semiconductor interfaces.[1–3] Indium phosphide (InP) is one of the fascinating semiconductor materials for development of high-speed optoelectronic and high-power microwave devices, due to its direct bandgap transition, high electron mobility, high saturation velocity, and high breakdown voltage.[4,5] However, it is critical to achieve barrier height (BH) above 0.5 eV for InP-based devices[6–8] due to the high density of surface states and other nonstoichiometric defects. Such defects lead to low BH, resulting in huge leakage current in diodes. This can be overcome by inclusion of an organic film between the metal and semiconductor, converting the MS junction into a metal/interlayer/semiconductor (MIS) junction. This increases the BH as the interfacial layer acts as a tunneling barrier.[9–11] Thus, formation of organic

(Received February 5, 2017; accepted May 19, 2017; published online June 20, 2017)

films on InP surfaces and investigation of their electrical properties are very important research issues. Different research groups have attempted to form thin organic films on *p*-type InP semiconductor and explored their electrical properties[12–21]; For instance, Aydin et al.[17] presented the electrical parameters of an Al/poly(3,4-ethylenedioxythiophene):poly(styrenesulfonate) (PEDOT:PSS)/*p*-InP diode, reporting higher BH and ideality factor of 0.98 eV (*I–V*) and 2.6 compared with the values of 0.83 eV and 1.13 for a reference Al/*p*-InP diode. Gullu et al.[18] prepared Ag/deoxyribonucleic acid (DNA)/*p*-InP structures and reported good rectifying behavior with increased barrier height. Kilicoglu et al.[19] estimated the ideality factor, BH, series resistance, and interface state density of an Al/tetrathiafulvalene (TTF)/*p*-InP/Au-Zn structure based on the *I–V* characteristic. Reddy et al.[20] proved that the Schottky barrier parameters of a Ti/*p*-InP Schottky diode were modified by inclusion of a polyaniline (PANI) organic interlayer and reported that higher barrier height was obtained for the Ti/polyaniline (PANI)/*p*-InP structure as compared with the Ti/*p*-InP structure. Recently, Padma et al.[21] reported the electrical and frequency-dependent properties of a Ti/polyethylene (PEO)/*p*-InP Schottky junction, finding that the BH was increased by 100 meV for the Ti/PEO/*p*-InP junction compared with the Ti/*p*-InP junction and pointing out that the BH was modified by addition of the PEO interlayer.

In view of the above discussion, the main aim of this work was to prepare and characterize the electrical properties of a Ti/Orange G/*p*-InP metal/interlayer/semiconductor (MIS) Schottky junction with an organic dye (Orange G) interlayer between the semiconductor and metal. Recent findings have revealed that organic thin-film interlayers between a metal and semiconductor can be depleted to modify the interfacial properties, effectively influencing device repeatability, reliability, and stability. In this work, Orange G (OG) organic dye was selected because of its simple composition, environmental friendliness, and good response to humidity. However, little data are available in literature regarding electrical properties of OG.[22] Furthermore, it is suggest that OG may be an effective and feasible material for fabrication of organic Schottky devices and solar cells, due to its low cost and potential for large-area devices. OG with molecular formula $C_{16}H_{10}N_2O_7S_2Na_2$ [7-hydroxy-8-(phenylazo)-1,3-naphthalenedisulfonic acid disodium salt] is the distinctive aromatic azo compound used in the present work. The molecular structure of Orange G is presented in Fig. 1a. Recently, organic dyes have also attracted significant attention due to their great relevance to light-induced photoisomerization processes and potential use for reversible optical data storage.[23] In light of the above properties of OG, we fabricated a Ti/Orange G (OG)/*p*-InP MIS junction and explored its electrical and current transport properties based on current–voltage (*I–V*) and capacitance–voltage (*C–V*) characteristics in the dark at room temperature. The electrical parameters of the Ti/OG/*p*-InP MIS junction were compared with those of a Ti/*p*-InP Schottky junction. In addition, the forward and reverse conduction mechanisms of the Ti/*p*-InP and Ti/OG/*p*-InP MIS junctions are reviewed and discussed in detail.

EXPERIMENTAL PROCEDURES

Ti/*p*-InP metal/semiconductor (MS) and Ti/Orange G/*p*-InP metal/interlayer/semiconductor (MIS) Schottky junctions were fabricated on one-side-polished *p*-type InP substrate (as received from manufacturer) with (100) orientation. The doping concentration was about 4×10^{17} cm^{-3} to 8×10^{17} cm^{-3} according to Hall measurements. First, to eradicate the damaged surface layer and unwanted impurities from the surface, the *p*-type InP substrate was dipped in $5H_2SO_4 + H_2O_2 + H_2O$ solution for 1 min. Then, the substrate was etched in HF:H_2O (1:10) solution for 1 min to eliminate native oxide from the surface. After that, the substrate was rinsed in deionized (DI) water and dried in high-purity nitrogen (N_2) gas flow. Platinum (Pt, 20 nm thickness) was deposited on the back side of the *p*-type InP substrate to form ohmic contacts, then annealed at 350°C for 1 min in N_2 environment using a rapid thermal annealing (RTA) system. Second, Orange G (OG) powder was

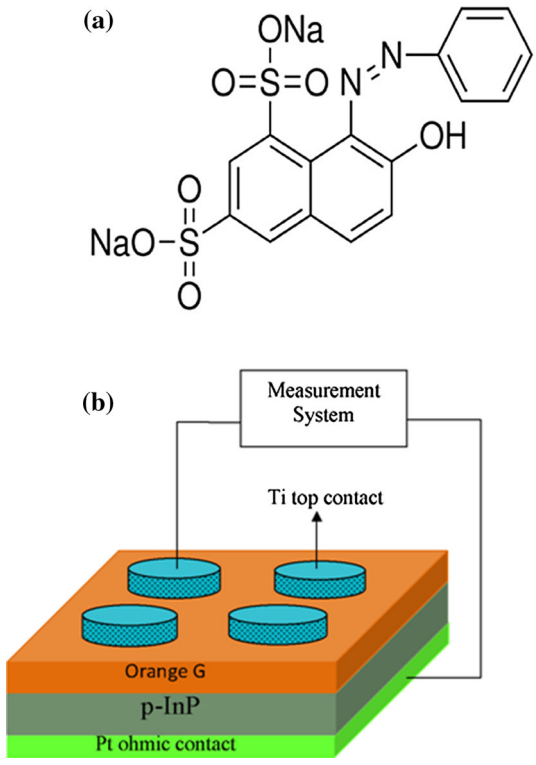

Fig. 1. (a) Molecular structure of Orange G organic dye. (b) Schematic of Ti/OG/*p*-InP MIS junction.

dissolved in DI water for 2 h. The OG solution was then directly applied onto the cleaned smooth surface of the *p*-InP substrate by spin coating (Laurell spin coater model no. WS-650 MZ-23NPP) at 4000 rpm for 60 s. The samples were dried in N_2 ambient for 1 h. The thickness of the OG film was determined to be 40 nm using a profilometer. Finally, Schottky dots with diameter of 0.7 mm were formed by evaporating titanium (Ti, 50 nm) through a stainless-steel mask onto the OG/*p*-InP using an e-beam evaporation system at pressure of 1.3×10^{-6} mbar. An MS junction was also prepared using similar conditions but without the OG film, to compare its electrical parameters with those of the MIS junction. A schematic of the prepared Ti/OG/*p*-InP MIS junction is presented in Fig. 1b. The current–voltage (*I*–*V*) and capacitance–voltage (*C*–*V*) characteristics of the Ti/*p*-InP and Ti/OG/*p*-InP MIS junctions were measured using a Keithley source measuring unit 2400 and automated deep-level transient spectroscopy (DLTS, DLS-83D) system under dark conditions.

RESULTS AND DISCUSSION

Typical current–voltage (*I*–*V*) characteristics of the Ti/*p*-InP metal/semiconductor (MS) and Ti/OG/*p*-InP metal/interlayer/semiconductor (MIS) junctions are illustrated in Fig. 2. Higher current rectification ratio was achieved for the MIS junction (1234) compared with the MS junction (40). As seen in Fig. 2, the reverse leakage current of the MIS junction (4.306×10^{-10} A at 1 V) was lower than that of the MS junction (2.419×10^{-7} A at 1 V), confirming that the OG organic dye layer formed a physical barrier between the metal and semiconductor. This indicates that the electrical properties of the MS junction were enhanced after inclusion of the OG interlayer. Thermionic emission (TE) theory[24] was employed to assess the *I*–*V* characteristics of the MS and MIS junctions. The current across a junction with series resistance can be expressed based on TE theory as

$$I = AA^{*}T^{2}\exp\left(-\frac{q\phi_b}{kT}\right)\exp\left(\frac{q(V-IR_S)}{nkT}\right) \quad (1)$$
$$\text{with } I_0 = AA^{*}T^{2}exp\left(-\frac{q\phi_b}{kT}\right),$$

where V is the voltage applied across the junction, IR_S is the voltage drop across the series resistance of the diode, q is the electronic charge, k is Boltzmann's constant, T is the absolute temperature in Kelvin, n is the ideality factor, ϕ_b is the zero-bias barrier height, A is the diode area, A^* is the effective Richardson constant (60 A cm^{-2} K^{-2} for *p*-InP[25]), and I_0 is the reverse saturation current determined as the intercept of a plot of ln I versus V at $V = 0$. The ideality factor was assessed from the slope of the linear region of forward-bias *I*–*V* curves. The barrier height (BH) can be estimated once I_0 has been determined. The BH and ideality factor were found to be 0.83 eV and 1.25, and 0.94 eV and 1.91 for the Ti/*p*-InP MS and Ti/OG/*p*-InP MIS junctions. Obviously, it can be stated that the BH and ideality factor obtained for the Ti/OG/*p*-InP MIS junction are adequate in comparison with values reported for other organic–inorganic devices.[17–21] Clearly, these results indicate that the BH is higher for the MIS junction compared with the MS junction, which can be attributed to the presence of the OG interlayer between the metal and semiconductor. Indeed, the BH of the MS junction modified by the OG layer indicates that the OG layer altered the space-charge region of the semiconductor.[26] Ultimately, the OG layer provides a physical barrier that prevents direct contact between the metal and the *p*-InP surface. In general, experimentally fabricated Schottky junctions exhibit ideality factors greater than unity. Our MS and MIS junctions showed ideality factors larger than one, which may occur due to the following effects: (1) interface states, (2) image force lowering, (3) fabrication-induced defects, (4) barrier inhomogeneities, and (5) nonuniformity of the interfacial layer formed at the MS junction.[27,28] Another reason for the higher ideality factor of the Ti/OG/*p*-InP MIS junction may be adjustment of the metal-induced gap states and bias voltage dependence of the BH.[29,30]

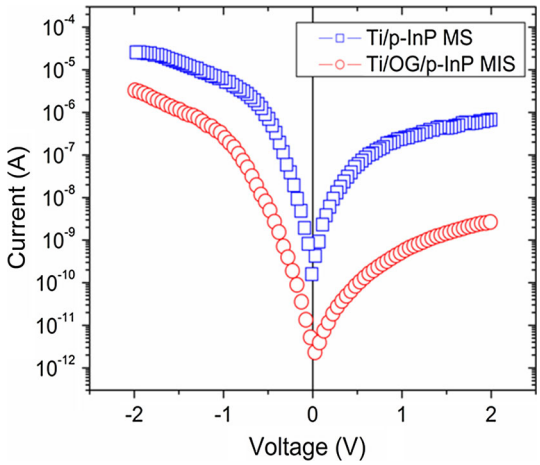

Fig. 2. Forward and reverse current–voltage (*I*–*V*) characteristics of Ti/*p*-InP MS and Ti/OG/*p*-InP MIS junctions.

Moreover, one should consider a few key factors to determine the device reliability and efficiency, including the series resistance (R_S) and shunt resistance (R_{Sh}) of the junction. Low R_S ensures high current flow across the junction, whereas R_{Sh} close to infinity ensures small leakage current across the junction. The R_S and R_{Sh} values were derived from plots of junction resistance ($R_j = \partial V/\partial I$) versus bias voltage for the MS and MIS junctions as shown in Fig. 3a and b. In the forward-bias region, the lower region of the R_j versus V plot corresponds to the value of R_S, while in the reverse-bias region,

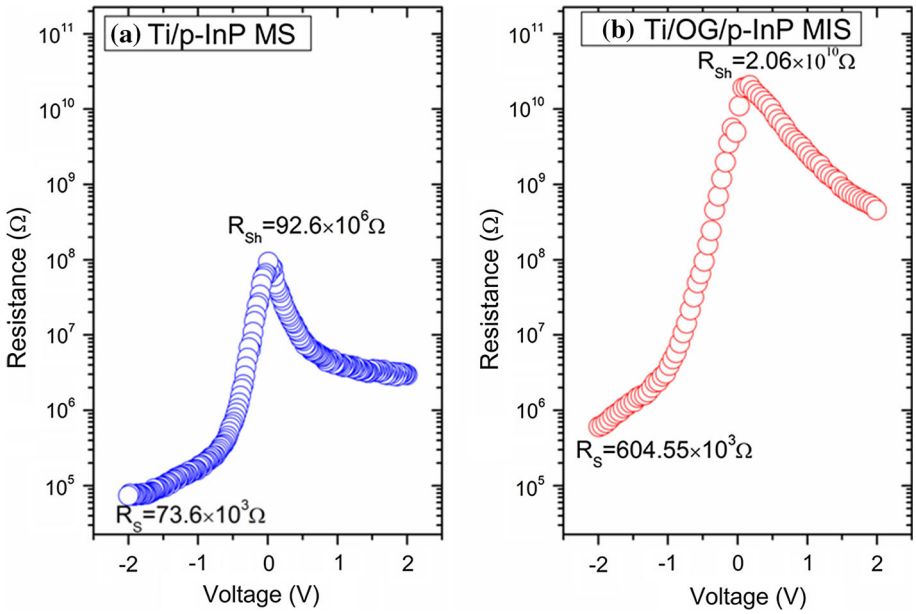

Fig. 3. Junction resistance (R_j) versus voltage (V) for (a) Ti/*p*-InP MS junction and (b) Ti/OG/*p*-InP MIS junction.

the maximum peak resistance is identified as R_{Sh}. From Fig. 3a and b, the R_S and R_{Sh} values were found to be 73.6 × 10^3 Ω and 92.6 × 10^6 Ω for the MS and 604.55 × 10^3 Ω and 2.06 × 10^{10} Ω for the MIS junction, respectively.

Furthermore, due to the influence of the series resistance (R_S) and interface states, the forward-bias I–V characteristics of the MS and MIS junctions departed from linearity at sufficiently high voltage. Therefore, the ideality factor, BH, and R_S were estimated from the nonlinear region for the MS and MIS junctions based on the technique developed by Cheung.[31] Cheung's functions can be expressed as

$$\frac{dV}{d(\ln I)} = \frac{nkT}{q} + IR_S, \tag{2}$$

$$H(I) = V - \left(\frac{nkT}{q}\right)\ln\left(\frac{I}{AA^*T^2}\right), \tag{3}$$

where $H(I)$ is given as follows:

$$H(I) = n\phi_b + IR_S. \tag{4}$$

Figure 4a and b present plots of dV/d(ln I) versus I and $H(I)$ versus I for the MS and MIS junctions. According to Eq. 2, the dV/d(ln I) versus I plot (Fig. 4a) is linear with slope of R_S, while its y-intercept gives the ideality factor n. The R_S and ideality factor estimated for the MS and MIS junctions [from the dV/d(ln I) versus I plot] were 99 kΩ and 2.21, and 248 kΩ and 3.79, respectively. The plots of $H(I)$ versus I obtained by substituting the ideality factors estimated using Eq. 3 into Eq. 4 are presented in Fig. 4b. This plot gives a straight line with slope of R_S and y-intercept of $n\phi_b$. From the $H(I)$ versus I plot, the R_S and ϕ_b values were found to be 83 kΩ and 0.82 eV for the MS junction and 322 kΩ and 0.88 eV for the MIS junction, respectively. The R_S values found from the dV/d(ln I)-V plot are nearly equal to those found from the H(I) versus I plot, implying that Cheung's functions are consistent and valid. These results indicate that the ϕ_b value determined from the $H(I)$ versus I plot closely matches those determined from the forward-bias ln(I) versus V plot. Nevertheless, the ideality factor estimated from the dV/d(ln I) versus I plot differs somewhat from those estimated from the forward-bias ln(I) versus V plot. The reason may be that both R_S and the interfacial properties influence the I–V characteristic, whereas only R_S influences the dV/d(ln I) versus I plot.[26,32,33]

The BH and R_S values for the Ti/*p*-InP MS and Ti/OG/*p*-InP MIS junctions were also derived by applying the modified Norde function,[34] expressed as

$$F(V) = \frac{V}{\gamma} - \frac{kT}{q}\ln\left(\frac{I(V)}{AA^*T^2}\right), \tag{5}$$

where $I(V)$ is the current determined from the I–V experimental data, and γ is an arbitrary dimensionless integer (which should be greater than the ideality factors derived from ln(I) versus V characteristics). Figure 5 shows a plot of the Norde function against the forward applied voltage (V) for the MS and MIS junctions according to Eq. 5. The BH was extracted using the following equation:

$$\phi_b = F(V_0) + \frac{V_0}{\gamma} - \frac{kT}{q}, \tag{6}$$

where $F(V_0)$ is the minimum point of $F(V)$ and V_0 is the corresponding voltage. Also, the R_S value can be extracted using the following relation:

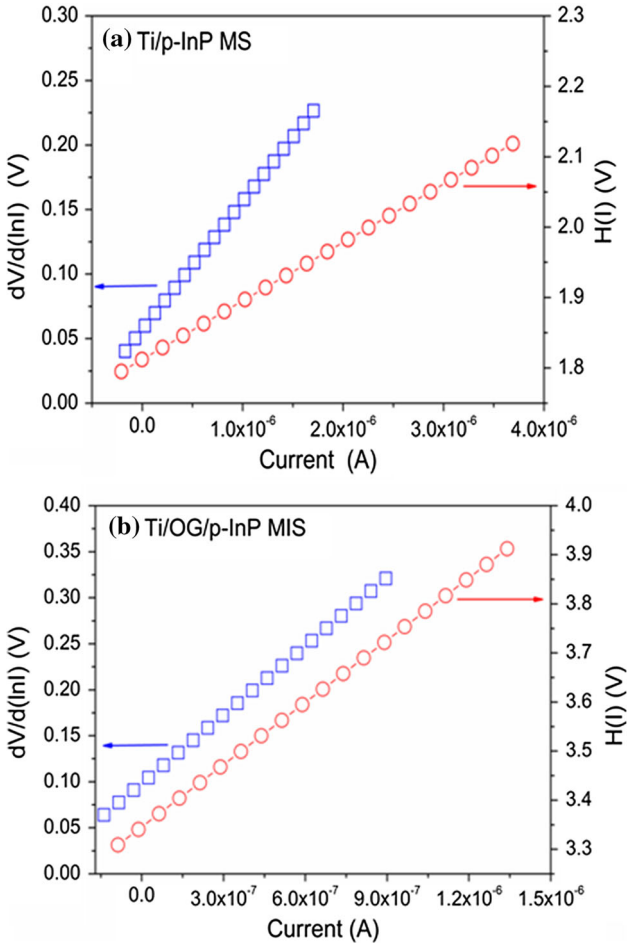

Fig. 4. Plots of dV/d(ln I) versus I and $H(I)$ versus I for the (a) Ti/p-InP MS junction and (b) Ti/OG/p-InP MIS junction.

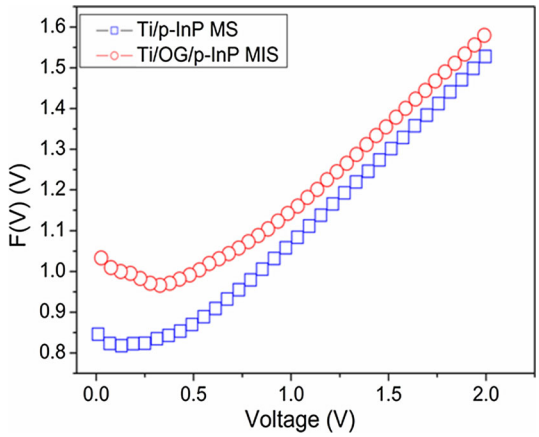

Fig. 5. $F(V)$ versus V plots for the Ti/p-InP MS and Ti/OG/p-InP MIS junctions.

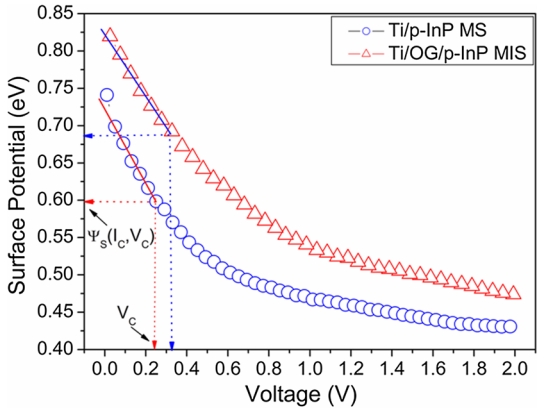

Fig. 6. Surface potential versus forward-bias voltage plots for Ti/p-InP MS and Ti/OG/p-InP MIS junctions.

$$R_S = \frac{kT(\gamma - n)}{qI_0}, \tag{7}$$

where I_0 corresponds to the minimum point $F(V_0)$. The BH and R_S values extracted in this way from the $F(V_0)$ versus V plot were 0.85 eV and 2.98 MΩ for the Ti/p-InP MS junction and 0.92 eV and 3.48 MΩ for the Ti/OG/p-InP MIS junction, respectively. The R_S values extracted using Cheung's method were lower than those extracted using Norde's function, which may be due to the different region of the I–V characteristic used, as Cheung's functions are applied in the nonlinear region while the Norde function uses the complete range of the forward-bias I–V characteristic.[33,35]

Taking into account the native insulating layer present on the semiconductor surface, the current through a metal/semiconductor junction can be described as[24]

$$I = AA^*T^2 \exp\left(-\frac{q\Psi_S}{kT}\right)\left[\exp\left(-\frac{qV_P}{nkT}\right)\right]. \tag{8}$$

Furthermore, the BH can also be extracted if the critical surface potential, $\Psi_S(I_C, V_C)$, critical voltage V_C, and $n = 1/\alpha$ values can be identified practically.[36] The surface potential Ψ_S is described as

$$\Psi_S = \frac{kT}{q} ln\left(\frac{AA^*T^2}{I}\right) - V_P, \tag{9}$$

where $V_P = kT/q\ln(N_v/N_a$ with N_a being the carrier concentration $[N_a = 2(2\pi m^* kT/h^2)^{3/2}$ with $m^* = 0.078m_0]$ and N_v the effective density of the valance band ($N_v = 1.1 \times 10^{19}$ cm^{-3} for p-InP[37]), which is related to the voltage variation between the Fermi level and the top of the valance band in the neutral region of p-InP. The potential difference Ψ_S is extracted by using the V_P values for the MS and MIS junctions. The resulting Ψ_S versus forward-bias voltage (V) plots for the MS and MIS junctions are shown in Fig. 6. The barrier height (ϕ_b) can be defined as

$$\phi_b = \Psi_S(I_c, V_c) + C_2V_c + V_P. \tag{10}$$

According to the Ψ_S versus V plot, the surface potential (Ψ_S) decreases linearly with V until a critical voltage (V_C) is reached, after which the voltage drop across R_S becomes equal to the applied potential and $\Psi_S(I_C, V_C)$ corresponds to the respective surface potential. The difference becomes extremely nonlinear when V exceeds V_C. The α value can be extracted using the following equation:

$$-\alpha = \left(\frac{d\Psi_S}{dV}\right)_{I_C,V_C}. \quad (11)$$

The critical V_C and $\Psi_S(I_C,V_C)$ values can be estimated from the plots for the MS and MIS junctions. Using Eqs. 10 and 11, the BH and ideality factor values were calculated to be 0.83 eV and 2.04, and 0.94 eV and 2.30 for the MS and MIS junction, respectively. Note that the BH values extracted from the forward-bias *I–V* characteristc, Cheung's function, Norde's technique, and the Ψ_S versus V plot are comparable to one another, indicating that the methods applied are reliable and valid.

The capacitance–voltage (*C–V*) characteristic of the Ti/*p*-InP MS and Ti/OG/*p*-InP MIS junctions was also measured at frequency of 1 MHz in the dark. Figure 7 depicts the reverse-bias C^{-2} versus V plot for the MS and MIS junctions, revealing linear behavior. Hence, the depletion layer capacitance can be represented as[24]

$$\frac{1}{C^2} = \left(\frac{2}{\varepsilon_s q N_a A^2}\right)\left(V_{bi} - \frac{kT}{q} - V\right), \quad (12)$$

where ε_s is the permittivity of the semiconductor *p*-InP ($\varepsilon_s = 12.4\varepsilon_0$, where ε_0 is the dielectric constant of free space of 8.85×10^{-14} F/cm), A is the area of the diode, q is the electron charge, and N_a is the carrier concentration. V_{bi} is the built-in potential, given by the equation $V_{bi} = V_0 + kT/q$, where V_0 is determined from the *x*-intercept of the plot of C^{-2} versus V and T is the absolute temperature. Then, the BH can be determined from the relation $\phi_b(C–V) = V_{bi} + V_p$. The built-in potential was thereby determined to be 0.85 V and 0.96 V for the MS and MIS junction, respectively. The BH of the MS and MIS junctions was extracted as 0.96 eV and 1.07 eV, respectively. The barrier height, ideality factor, series resistance, and shunt resistance values for the Ti/*p*-InP MS and Ti/OG/*p*-InP MIS junctions extracted based on the *I–V* characteristic, Cheung's and Norde's methods, and the Ψ_S–*V* and *C–V* characteristics are summarized in Table I. As seen from the values in this table, the BH values obtained using the *I–V* and *C–V* techniques were quite different from one another for both the MS and MIS junctions, which may be due to the different nature of the *I–V* and *C–V* techniques. Also, the following reasons could explain the different BH values obtained using the *I–V* and *C–V* methods: (1) nonuniformity of the interfacial layer thickness, (2) the distribution of interface charges,

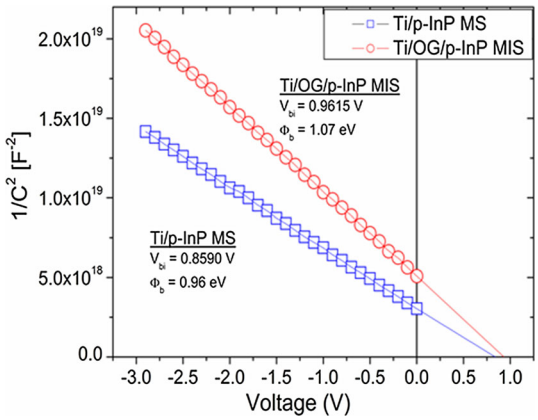

Fig. 7. Plots of $1/C^2$ versus V for the Ti/*p*-InP MS and Ti/OG/*p*-InP MIS junctions.

(3) deep impurity levels, (4) image-force barrier lowering, (5) barrier inhomogeneities, and (6) edge leakage currents.[38–40]

Moreover, the density distribution of interface states can be extracted from the forward-bias *I–V* characteristic by considering the voltage-dependent ideality factor and effective BH. Using the model proposed by Card and Rhoderick,[41] the interface state density (N_{SS}) is defined as

$$N_{SS} = \frac{1}{q}\left[\frac{\varepsilon_i}{\delta}(n(V) - 1) - \frac{\varepsilon_s}{W_d}\right], \quad (13)$$

where W_d is the space-charge width, ε_s is the permittivity of the semiconductor, ε_i is the permittivity of the interlayer, δ is the thickness of the organic interlayer, and $n(V) = (q/kT)[V/\ln(I/I_0)]$ is the voltage-dependent ideality factor. For a *p*-type semiconductor, the energy of interface states (E_{SS}) with regard to the top of the valence band at the surface of the semiconductor is expressed as

$$E_{SS} - E_v = q(\phi_e - V), \quad (14)$$

where V and ϕ_e are the voltage drop across the depletion layer and the effective BH, respectively. Figure 8 shows the N_{SS} versus $E_{SS} - E_V$ curves for the MS and MIS junctions. The extracted N_{SS} values lie in the range from 4.544×10^{13} eV^{-1} cm^{-2} (0.53 eV $- E_V$) to 6.38×10^{12} eV^{-1} cm^{-2} (0.81 eV $-E_V$) and from 3.731×10^{12} eV^{-1} cm^{-2} (0.58 eV $- E_V$) to 6.637×10^{11} eV^{-1} cm^{-2} (0.92 eV $- E_V$) for the Ti/*p*-InP MS and Ti/OG/*p*-InP MIS junction, respectively. Note that N_{SS} rises exponentially from midgap with respect to the top of the valence band. The extracted N_{SS} value for the MIS junction is less than that found for the MS junction, demonstrating that the OG interlayer is efficient in reducing N_{SS}. These results prove that the OG interlayer leads to considerable modification of the interface states, even though the OG/*p*-InP interface appears to be abrupt and unreactive.[2,42] The presence of a thin interfacial layer separating semiconductor and

Table I. Extracted barrier height, ideality factor, shunt resistance, and series resistance for the Ti/*p*-InP MS and Ti/OG/*p*-InP MIS junctions

Parameter	Ti/*p*-InP	Ti/OG/*p*-InP
From *I*–*V* characteristic		
Barrier height, ϕ_b (eV)	0.83	0.94
Ideality factor, n	1.25	1.91
Series resistance, R_S (Ω)	73.6×10^3	604.55×10^3
Shunt resistance, R_{Sh} (Ω)	92.6×10^6	2.06×10^{10}
Cheung's method		
Using d*V*/d(ln *I*) versus *I*		
Series resistance, R_S (kΩ)	99	248
Ideality factor, n	2.21	3.79
Using *H*(*I*) versus *I*		
Series resistance, R_S (kΩ)	82	322
Barrier height, ϕ_b (eV)	0.82	0.88
Norde's method		
Series resistance, R_S (MΩ)	2.98	3.48
Barrier height, ϕ_b (eV)	0.85	0.92
Using Ψ_S–*V* plot		
Barrier height, ϕ_b (eV)	0.83	0.94
Ideality factor, n	2.04	2.30
Using *C*–*V* characteristic		
Built-in potential (V)	0.85	0.96
Barrier height, ϕ_b (eV)	0.96	1.07

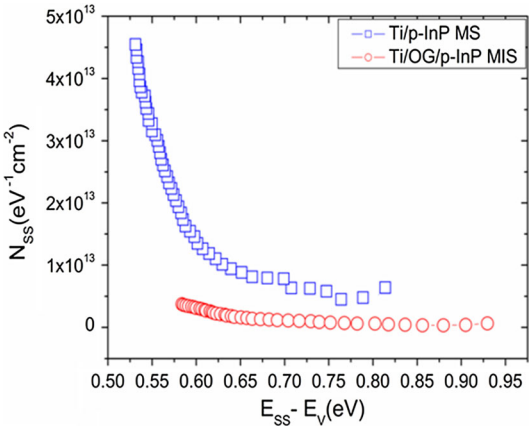

Fig. 8. Plots of N_{SS} versus $E_{SS} - E_v$ for the Ti/*p*-InP MS and Ti/OG/*p*-InP MIS junctions.

metal results in net charge of the gap states together with a corresponding image charge on the surface of the metal. As a result, a dipole layer is formed, which modifies the energy barrier and hence the BH depending on the surface state density.[43] Based on this analysis, it can be concluded that the OG organic layer plays an important role in decreasing N_{SS} and increasing the effective BH of the Ti/*p*-InP MS junction. The schematic band diagrams for the Ti/*p*-InP MS and Ti/OG/*p*-InP MIS junctions including the interface states and interfacial layer are presented in Fig. 9a and b.

To analyze the current conduction mechanism governing the reverse-bias *I*–*V* characteristic of the Ti/*p*-InP MS and Ti/OG/*p*-InP MIS junctions, the log of the reverse-bias current [ln(I_R)] is plotted against $V_R^{1/2}$ in Fig. 10 to determine whether Poole–Frenkel emission (PFE) or Schottky emission (SE) dominates at the junction. If the reverse-bias current is governed by Poole–Frenkel emission (PFE), it can be expressed as[44,45]

$$I_R = I_0 \exp\left(\frac{\beta_{PF} V^{1/2}}{kTd^{1/2}}\right), \tag{15}$$

whereas the Schottky emission (SE) mechanism is defined as

$$I_R = AA^*T^2 \exp\left(\frac{-\phi_b}{kT}\right) \exp\left(\frac{\beta_{SC} V^{1/2}}{kTd^{1/2}}\right), \tag{16}$$

where β_{PF} and β_{SC} are the PFE and SE field-lowering coefficients, respectively, and d is the film thickness. The theoretical values of β_{PF} and β_{SC} can be derived as follows:

$$2\beta_{SC} = \beta_{PF} = \left(\frac{q^3}{\pi\varepsilon_0\varepsilon_r}\right)^{1/2}, \tag{17}$$

where q is the electronic charge, ε_r is the relative permittivity of Orange G (i.e., $\varepsilon_r = 7$), and ε_0 is the permittivity of free space ($\varepsilon_0 = 8.85 \times 10^{-14}$ F/cm). Substituting the values of $\varepsilon_r\varepsilon_0$ into Eq. 17, the theoretical values of β_{PF} and β_{SC} can be calculated. The β_{PF} value is always double the value of β_{SC}. The theoretical values of β_{PF} and β_{SC} extracted for the Ti/*p*-InP MS and Ti/OG/*p*-InP MIS junctions were 2.15×10^{-5} eV m$^{1/2}$ V$^{-1/2}$ and 1.077×10^{-5} eV m$^{1/2}$ V$^{-1/2}$,

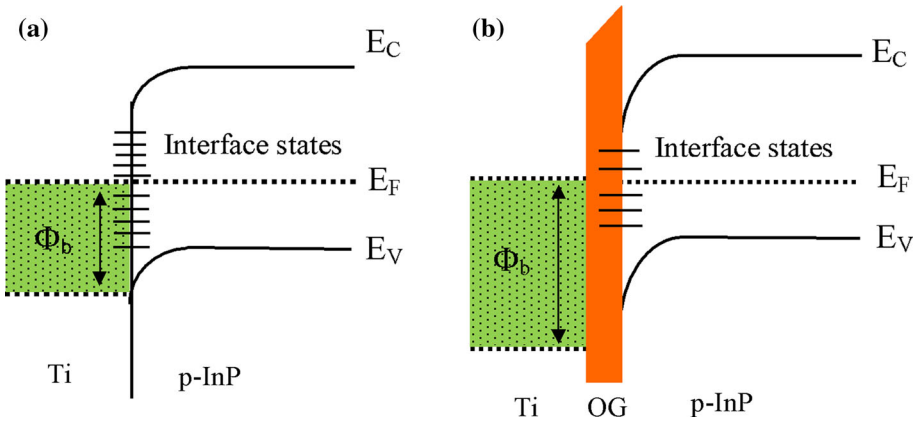

Fig. 9. Schematic energy band diagram of (a) Ti/*p*-InP MS junction and (b) Ti/OG/*p*-InP MIS junction.

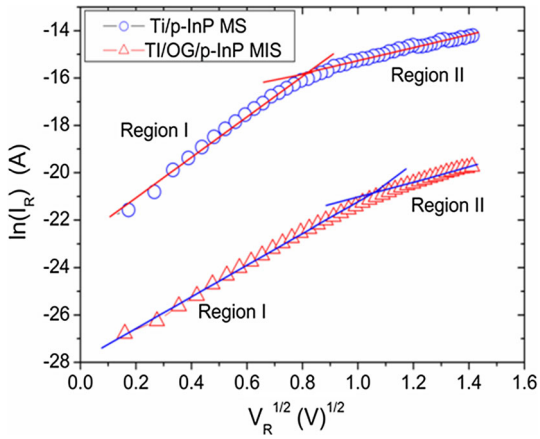

Fig. 10. Plots of $\ln(I_R)$ versus $V_R^{1/2}$ for the Ti/*p*-InP MS and Ti/OG/*p*-InP MIS junctions.

and 2.86×10^{-5} eV m$^{1/2}$ V$^{-1/2}$ and 1.43×10^{-5} eV m$^{1/2}$ V$^{-1/2}$, respectively. The plots of $\ln(I_R)$ versus $V_R^{1/2}$ for the MS and MIS junctions clearly show two different linear regions (I and II; Fig. 10). The experimentally obtained slope values for the Ti/*p*-InP MS and Ti/OG/*p*-InP MIS junctions were 6.1×10^{-5} eV m$^{1/2}$ V$^{-1/2}$ and 1.37×10^{-5} eV m$^{1/2}$ V$^{-1/2}$, and 5.35×10^{-5} eV m$^{1/2}$ V$^{-1/2}$ and 2.1×10^{-5} eV m$^{1/2}$ V$^{-1/2}$, respectively. The slope values extracted from region I (lower bias) of the plots for the MS and MIS junctions were close to the theoretical values of β_{PF}, while those extracted from region II were close to the theoretical values of β_{SC}. This analysis reveals that the reverse current conduction is governed by the Poole–Frenkel mechanism at lower bias but by Schottky emission at higher bias. In Schottky emission, current conduction takes place across the contact interface instead of the bulk material as a result of the nonuniformity and subatomic structure of the OG layer.[45] In the case of the Poole–Frenkel conduction mechanism, there is a wide distribution of traps in the bandgap of the OG layer, related to defects or impurities in its chemical structure. This high density of structural defects or trap levels enhances trapping/detrapping of charge carriers at the interface.[46]

CONCLUSIONS

The electrical properties and current transport mechanism of a Ti/OG/*p*-InP metal/interlayer/semiconductor (MIS) junction prepared with an Orange G (OG) interlayer were studied based on the *I–V* and *C–V* characteristics. The Ti/OG/*p*-InP MIS junction exhibited excellent rectification ratio in comparison with a Ti/*p*-InP metal/semiconductor (MS) junction. The MIS junction showed higher BH (0.94 eV from the *I–V* characteristic or 1.07 eV from the *C–V* characteristic) compared with the MS junction (0.83 eV from the *I–V* characteristic or 0.96 eV from the *C–V* characteristic), implying that inclusion of the OG layer influenced the potential barrier of the MS junction, thereby modifying the effective BH value. Also, the shunt resistance and series resistance were estimated for the MS and MIS junctions. The BH, ideality factor, and series resistance of the MS and MIS junctions were extracted by applying Cheung's and Norde's methods and from the Ψ_S–*V* plot. The BH values extracted by all three methods were comparable, indicating that the techniques applied were consistent and valid. The interface state density (N_{SS}) was lower for the MIS junction than for the MS junction, suggesting that addition of the OG organic layer led to decreased N_{SS} in the MS junction. The analysis results indicate that the reverse current mechanism in the lower bias region was regulated by Poole–Frenkel emission while Schottky emission dominated in the higher-bias region, for both the MS and MIS junctions. The results of this work demonstrate that the electrical parameters of the Ti/*p*-InP MS junction are substantially altered due to the presence of the Orange G (OG) organic layer. These exploratory results suggest that such junctions including an OG layer have potential for use in development of organic–inorganic devices.

REFERENCES

1. A.R.V. Roberts and D.A. Evans, *Appl. Phys. Lett.* 86, 072105 (2005).
2. T.U. Kampen, S. Park, and D.R.T. Zahn, *Appl. Surf. Sci.* 190, 461 (2002).
3. M. Cakar and A. Turut, *Synth. Met.* 138, 549 (2003).
4. Zs.J. Horvath, V. Rakovics, B. Szentpali, and S. Puspoki, *Phys. Status Solidi C* 0, 916 (2003).
5. P.G. McCafferty, A. Sellai, P. Dawson, and H. Elabd, *Solid-State Electron.* 39, 583 (1996).
6. Zs.J. Horvath, V. Rakovics, B. Szentpali, S. Puspoki, and K.Z. Ydansky, *Vacuum* 71, 113 (2003).
7. H. Cetin and E. Ayyildiz, *Semicond. Sci. Technol.* 20, 625 (2005).
8. V. Rajagopal Reddy, *Thin Solid Films* 556, 300 (2014).
9. T.S. Shafai, *Thin Solid Films* 3, 1200 (2008).
10. K.R. Rajesh and C.S. Menon, *J. Non Cryst. Solids* 4, 398 (2007).
11. O. Pakma, N. Serin, T. Serin, and S. Altindal, *J. Appl. Phys.* 104, 014501 (2008).
12. F.E. Jones, C. Daniels-Hafer, B.P. Wood, R.G. Danner, and M.C. Lonergan, *J. Appl. Phys.* 90, 1001 (2001).
13. S. Aydogan, M. Saglam, and A. Turut, *Vacuum* 77, 269 (2005).
14. S. Aydogan, M. Saglam, and A. Turut, *J. Polym. Sci. Part B Polym. Phys.* 44, 1572 (2006).
15. O. Gullu, A. Turut, and S. Asubay, *J. Phys.: Condens. Matter* 20, 045215 (2008).
16. O. Gullu, M. Cankaya, O. Baris, and A. Turut, *Appl. Phys. Lett.* 92, 212106 (2008).
17. M.E. Aydin and F. Yakuphanoglu, *Microelectron. Reliab.* 52, 1350 (2012).
18. O. Gullu, O. Pakma, and A. Turut, *J. Appl. Phys.* 111, 044503 (2012).
19. T. Kilicoglu, A. Tombak, Y.S. Ocak, and M. Aydemir, *Microelectron. Eng.* 129, 91 (2014).
20. P.R. Sekhar Reddy, V. Janardhanam, I. Jyothi, S.-H. Yuk, V. Rajagopal Reddy, J.-C. Jeong, S.-N. Lee, and C.-J. Choi, *J. Semicond. Technol. Sci.* 16, 664 (2016).
21. R. Padma, K. Sreenu, and V. Rajagopal Reddy, *J. Alloys Compd.* 695, 2587 (2017).
22. S.A. Moiz, M.M. Ahmed, and K.S. Karimov, *ETRI J.* 27, 319 (2005).
23. O. Gullu, M. Cankaya, M. Biber, and A. Turut, *J. Phys.: Condens. Matter* 20, 215210 (2008).
24. E.H. Rhoderick and R.H. Williams, *Metal-Semiconductor Contacts*, 2nd ed. (Oxford: Clarendon, 1988), p. 33.
25. R.H. Williams and G.Y. Robinson, *Physics and Chemistry of III-V Compound Semiconductor Interfaces*, ed. C.W. Wilmsen (New York: Plenum, 1985).
26. V. Rajagopal Reddy, M.S.P. Reddy, A.A. Kumar, and C.-J. Choi, *Thin Solid Films* 520, 5715 (2012).
27. B.L. Sharma, *Metal-Semiconductor Schottky Barrier Junctions and Their Applications* (New York, London: Plenum, 1984).
28. E. Maril, A. Kaya, S. Kocyigit, and S. Altindal, *Mater. Sci. Semicond. Process.* 31, 256 (2015).
29. R.T. Tung, *Phys. Rev. B* 45, 13509 (1992).
30. H. Cetin, B. Sahin, E. Ayylidiz, and A. Turut, *Phys. B* 364, 133 (2005).
31. S.K. Cheung and N.W. Cheung, *Appl. Phys. Lett.* 49, 85 (1986).
32. S. Karatas, S. Altindal, A. Turut, and M. Cakar, *Phys. B* 392, 43 (2007).
33. P. Prabhu Thapaswini, R. Padma, N. Balaram, B. Bindu, and V. Rajagopal Reddy, *Superlattices Microstruct.* 93, 82 (2016).
34. H. Norde, *J. Appl. Phys.* 50, 5052 (1979).
35. V. Rajagopal Reddy, B. Asha, and C.-J. Choi, *J. Electron. Mater.* 45, 3268 (2016).
36. P. Chattopadhyay, *Solid-State Electron.* 38, 739 (1995).
37. V. Rajagopal Reddy, D. Sri Silpa, H.-J. Yun, and C.-J. Choi, *Superlattices Microstruct.* 71, 134 (2014).
38. V. Rajagopal Reddy, D. Sri Silpa, V. Janardhanam, H.-J. Yun, and C.-J. Choi, *Electron. Mater. Lett.* 11, 73 (2015).
39. S.M. Sze, *Physics of Semiconductor Devices*, 2nd ed. (New York: Wiley, 1981).
40. Y.P. Song, R.L. Van Meirhaeghe, W.H. Laflare, and F. Cardon, *Solid-State Electron.* 29, 633 (1986).
41. H.C. Card and E.H. Rhoderick, *J. Phys. D* 4, 1589 (1971).
42. S.R. Forrest, M.L. Kaplan, and P.H. Schmidt, *J. Appl. Phys.* 60, 2406 (1986).
43. I. Jyothi, V. Janardhanam, Y.-R. Lim, V. Rajagopal Reddy, K.-S. Ahn, and C.-J. Choi, *Mater. Sci. Semicond. Process.* 30, 420 (2015).
44. A.S. Raid, *Phys. B* 270, 148 (1999).
45. A.C. Varghese and C.S. Menon, *Eur. Phys. J. B* 47, 485 (2005).
46. D.N. Khan and M.H. Sayyad, in *Second International Conference on Computer Research and Development* (Kuala Lumpur: 2010) p. 535.